The first IXPE view of the eclipsing ADC source 4U 1822–37

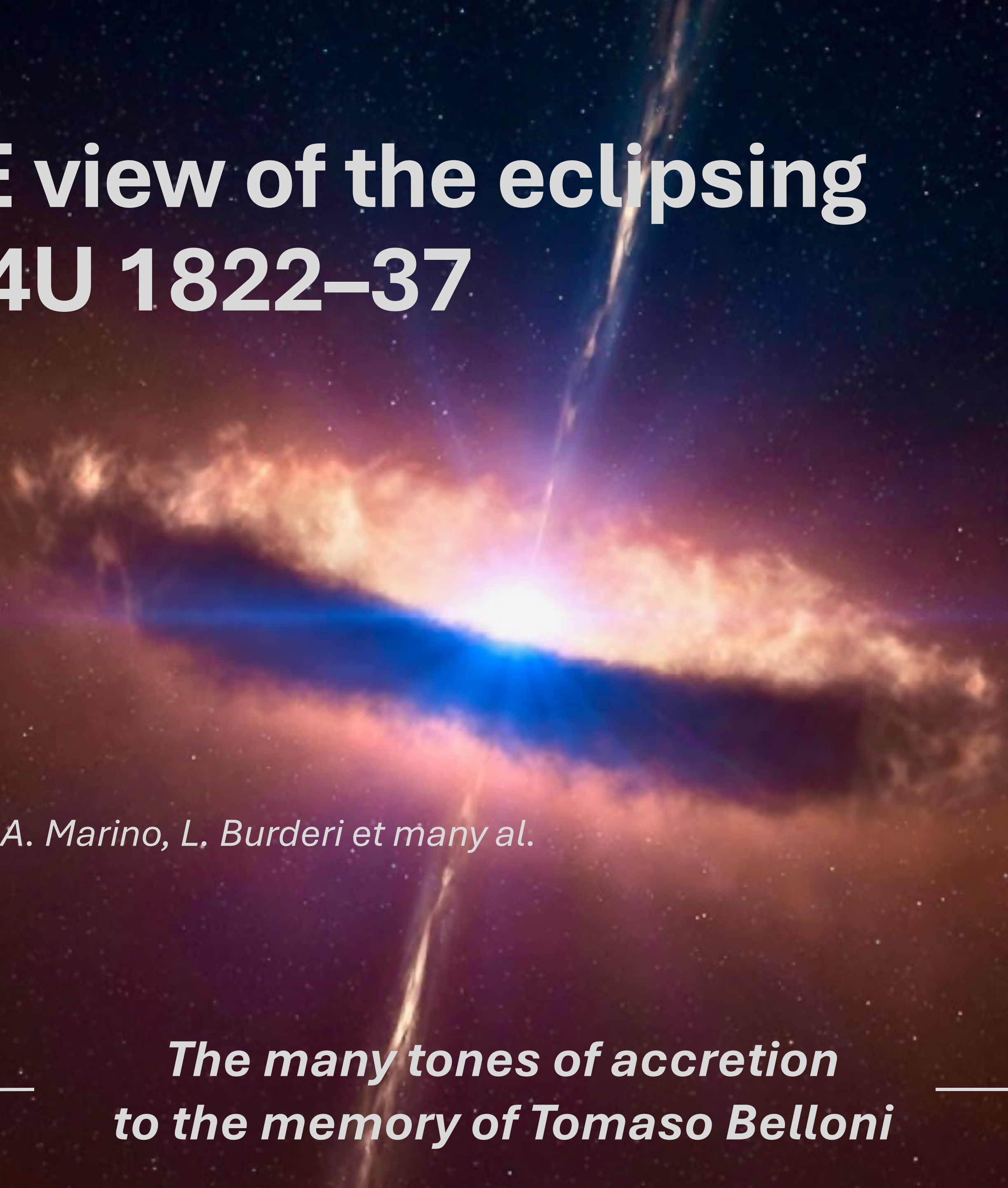

Alessio Anitra

Università degli studi di Palermo

INAF-IASF Palermo

A. Gnarini, T. Di Salvo, R. Iaria, A. Marino, L. Burderi et many al.

The many tones of accretion
to the memory of Tomaso Belloni

Spectroscopy and polarization

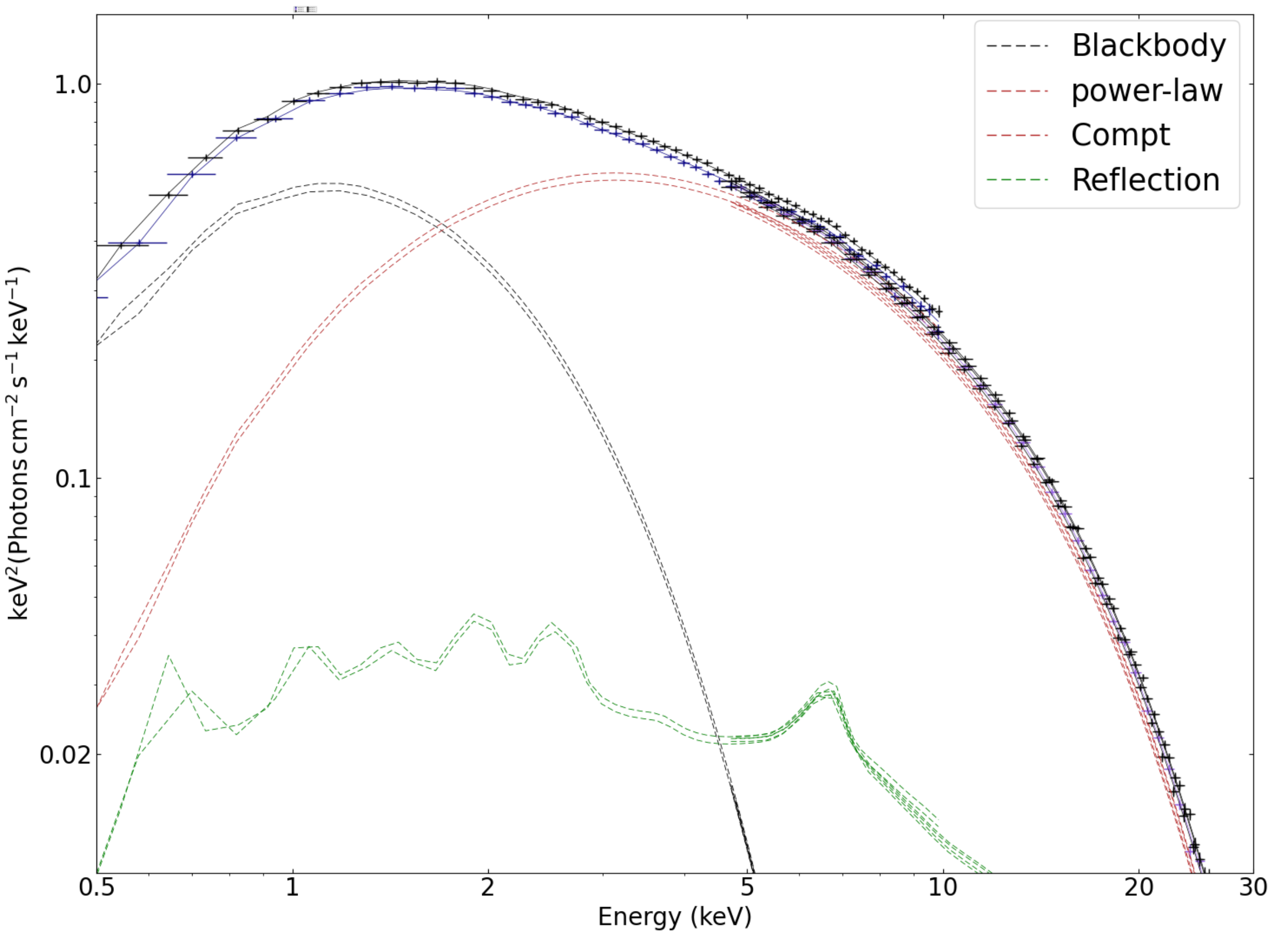

Example of LMXB spectrum

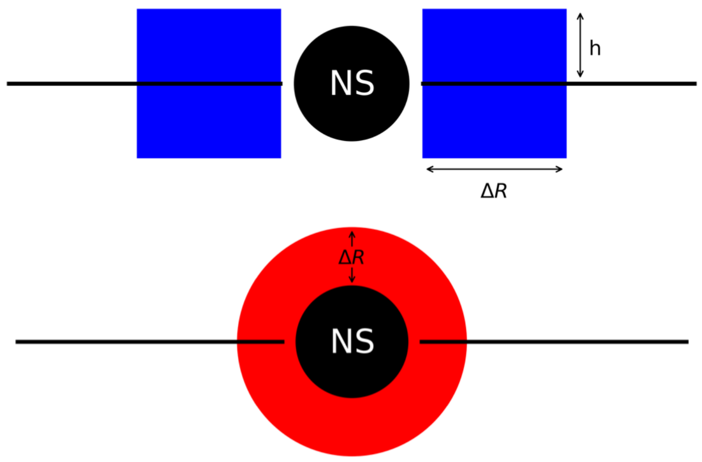

Schematic view of **Shell** and **Slab** Corona and the associated PD (**Adapted from Gnarini+2022**)

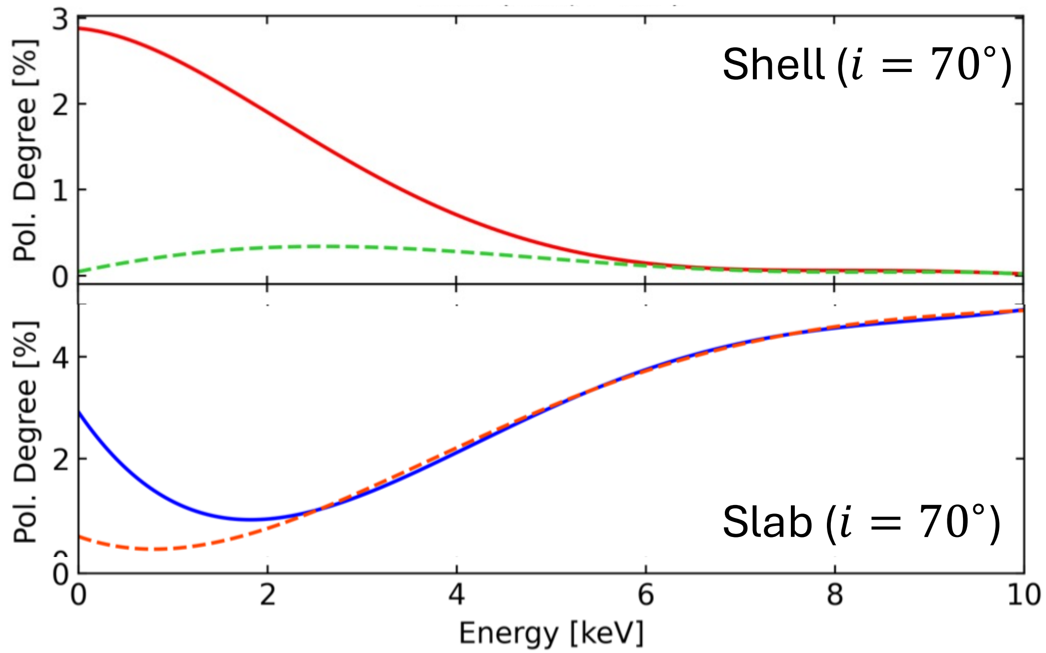

High inclination systems

Di Marco+2024.

In GX 13+1 during the dip the PD increases and the PA swings.

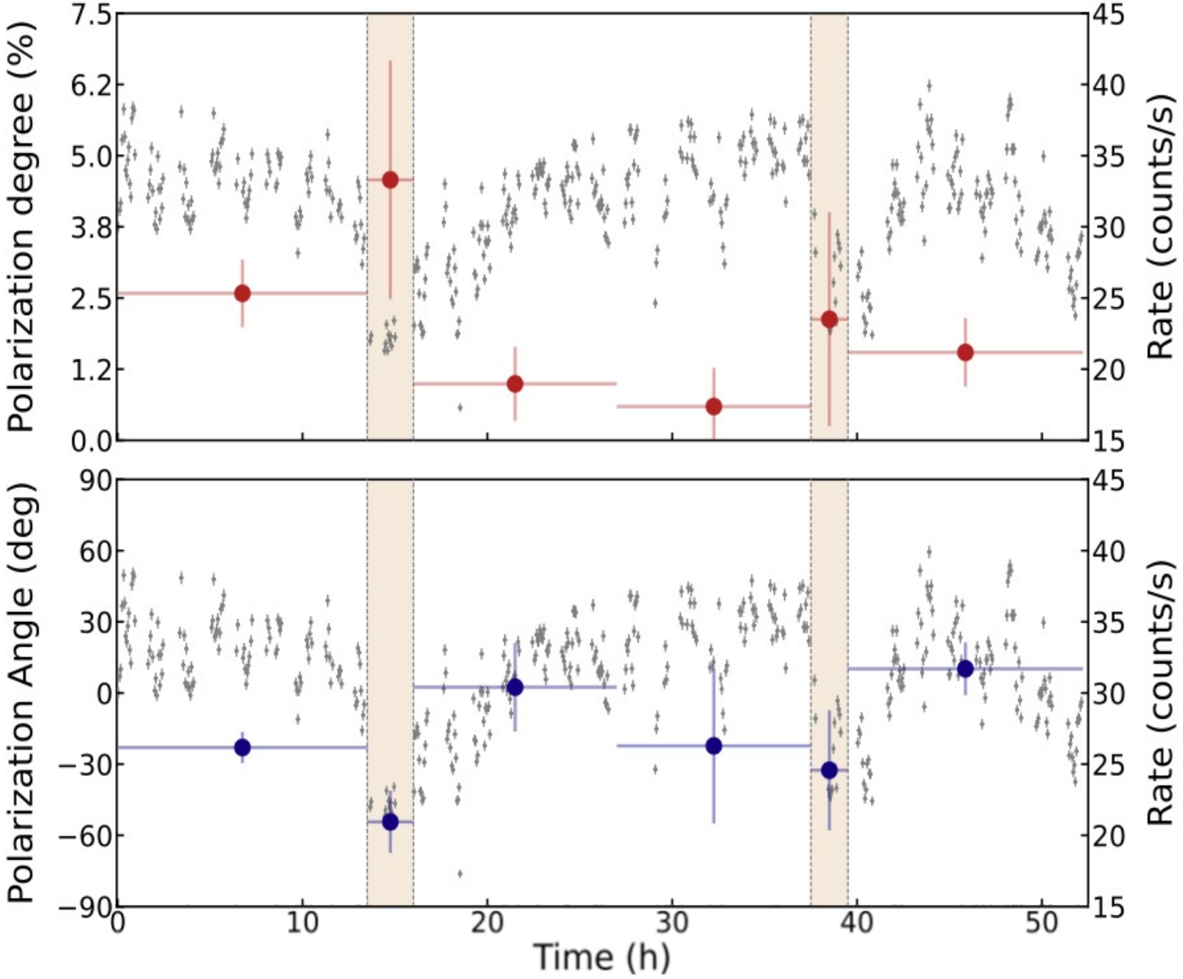

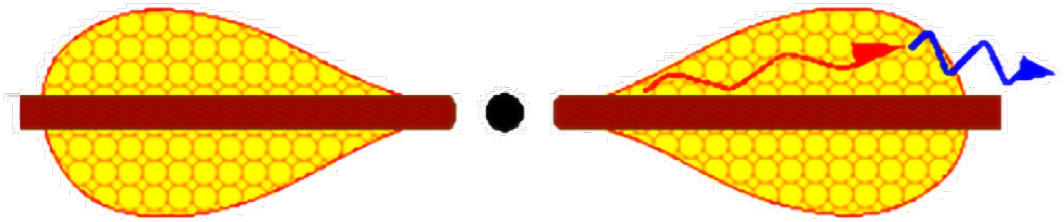

Sketch of ADC

- In high inclination systems scattered and reprocessed radiation becomes important and produces higher PD.

- **ADC sources :** observed emission produced by scattering in an extend sandwich-like corona.

The case of 4U 1822-37

Eclipsing ADC LMXB hosting a 0.59 s X-ray pulsar, viewed at $80° - 85°$.

Luminosity mismatch

The observed luminosity is only of order 10^{36}erg s^{-1}, but the intrinsic luminosity is close to the Eddington limit (10^{38}erg s^{-1}).

Large orbital period derivative implies super-Eddington mass transfer (**Burderi+2010**).

Ghosh & Lamb (1979) model:

Observed luminosity implies

$\mathrm{B} \sim 10^{16}$ G ✗

Eddington luminosity implies

$\mathrm{B} \sim 10^{11}$ G ✓

Cyclotron line at 0.66 keV (**Iaria+2024**)

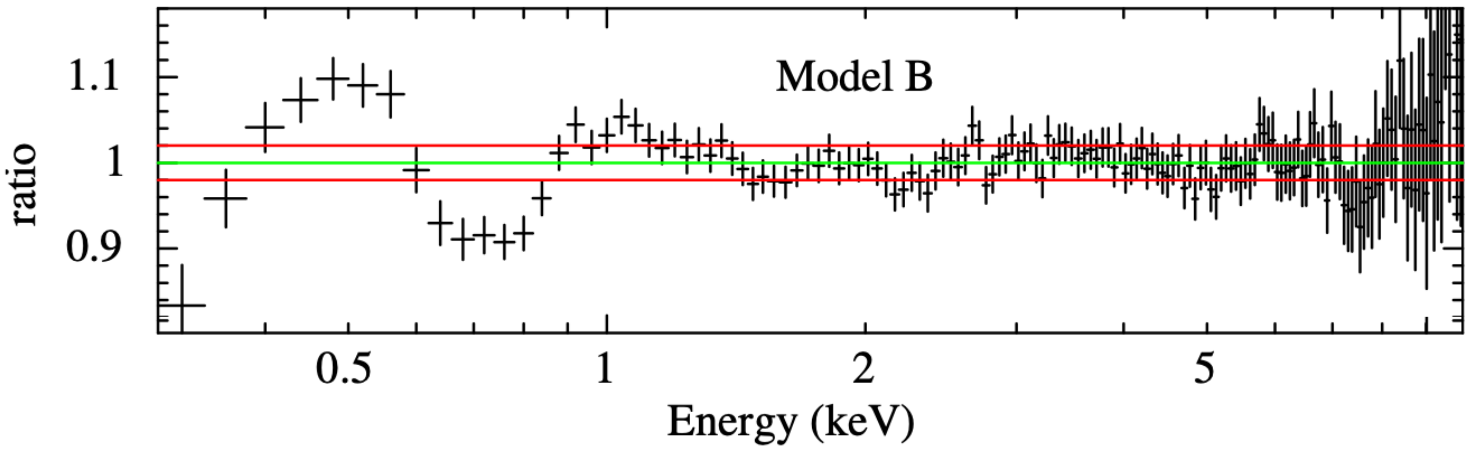

4U 1822–37 is intrinsically much brighter than it appears

The periscope scenario

We can still probe the inner regions.
Thermal emission,
Comptonization, Reflection
and X-ray pulsations
(Iaria+2013, 2024; Anitra+2021)

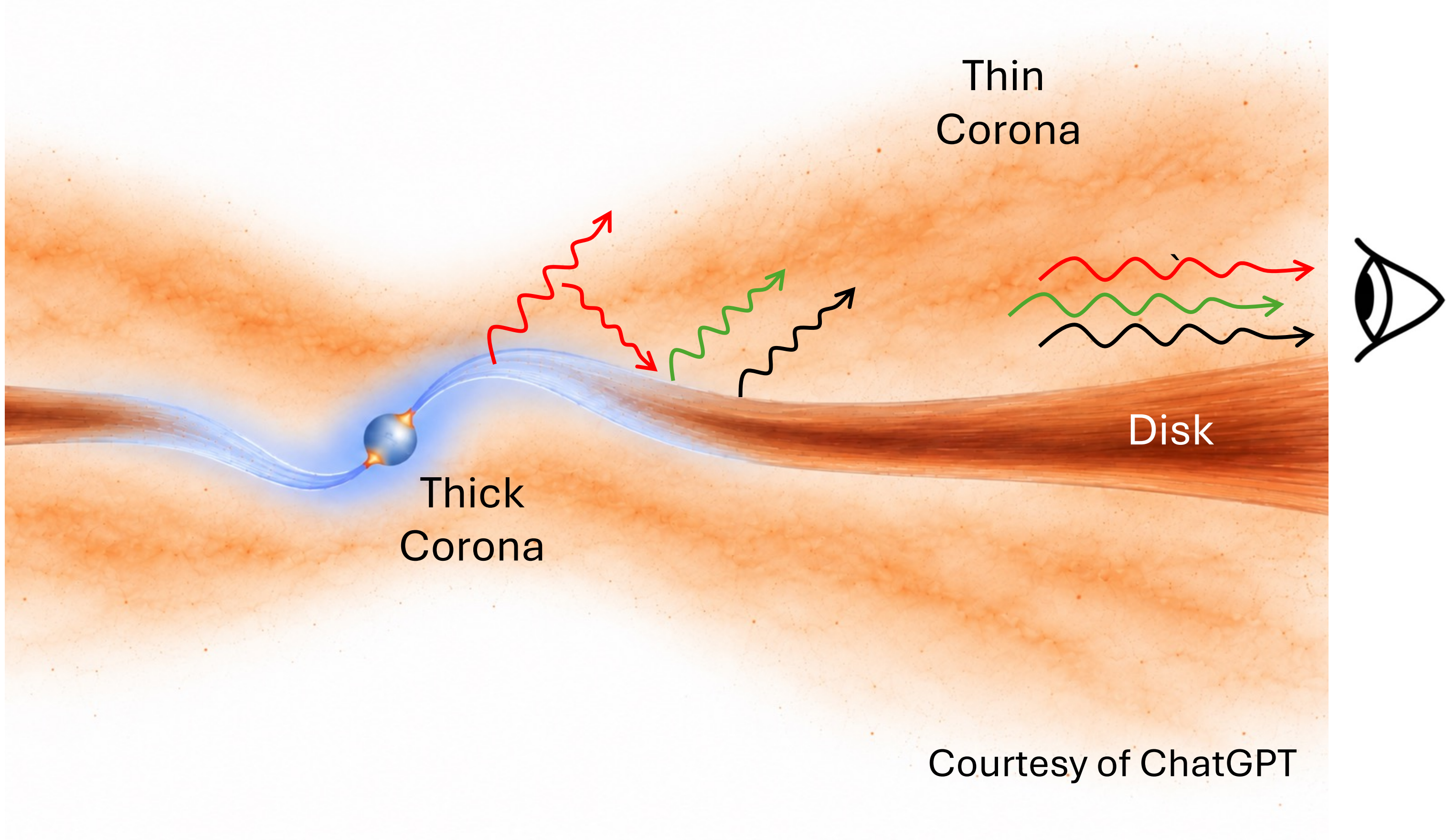

Periscope:
An extended, optically thin ADC scatters a small fraction of the intrinsic radiation into our line of sight.

Testing the geometry through a coordinated spectral and polarimetric campaign with XMM-Newton, Swift, NuSTAR, and IXPE

Spectral decomposition

Model = Tbabs × (4 Gaussian + bbodyrad + thcomp × bbodyrad +relconv × rfxconv + power−law)

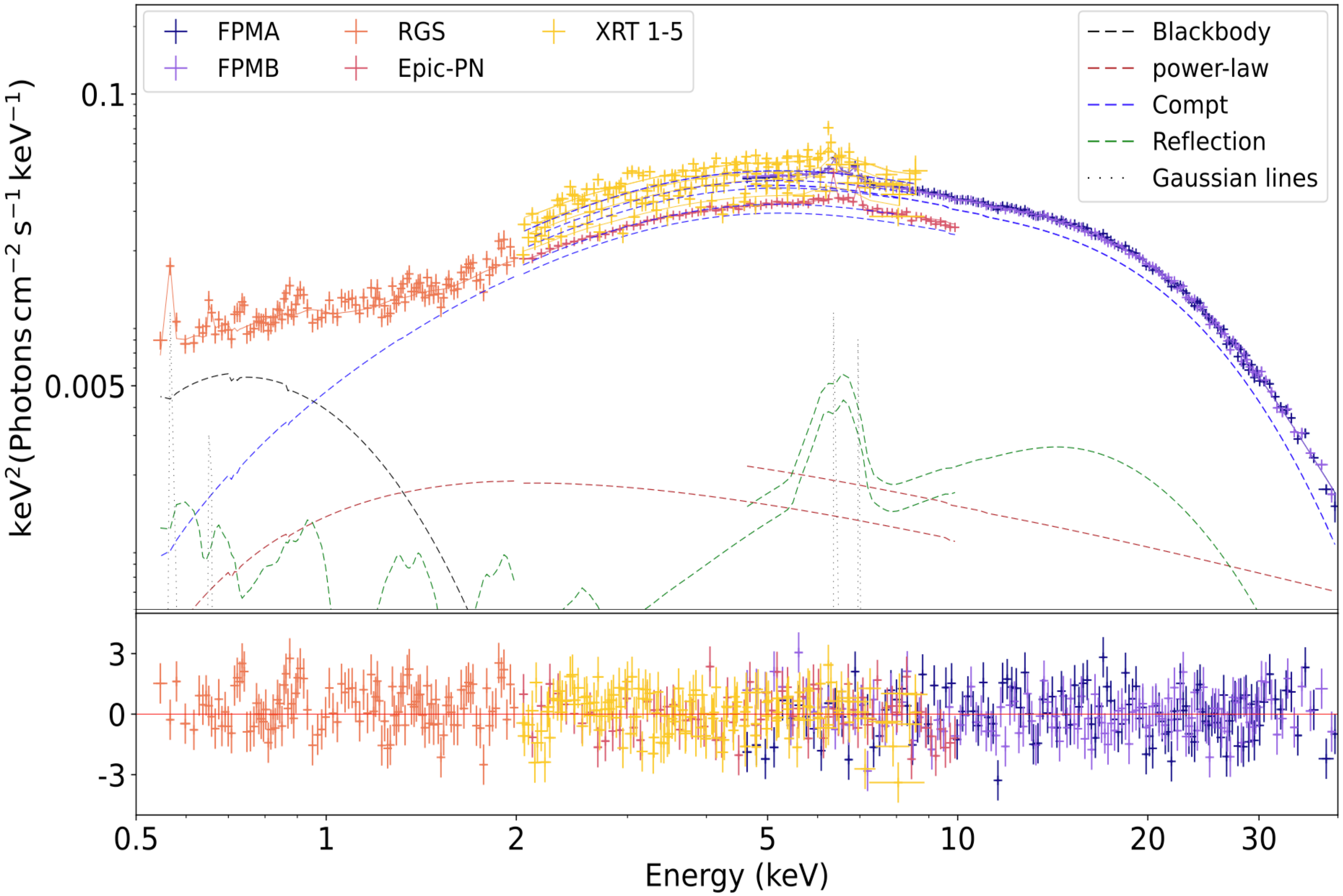

Consistent ADC picture

- **Blackbody** emitted from the inner part of the disc.
- **Seed photons** compatible with emission from the neutron-star surface.
- **Inner radius** consistent with a truncated disc at the magnetospheric radius.

Polarimetric analysis

PD = 8.0 % ± 0.7 % and PA = -21° ± 2°.

The PD increases with energy, reaching 11% in the 7–8 keV bin while the PA is stable.

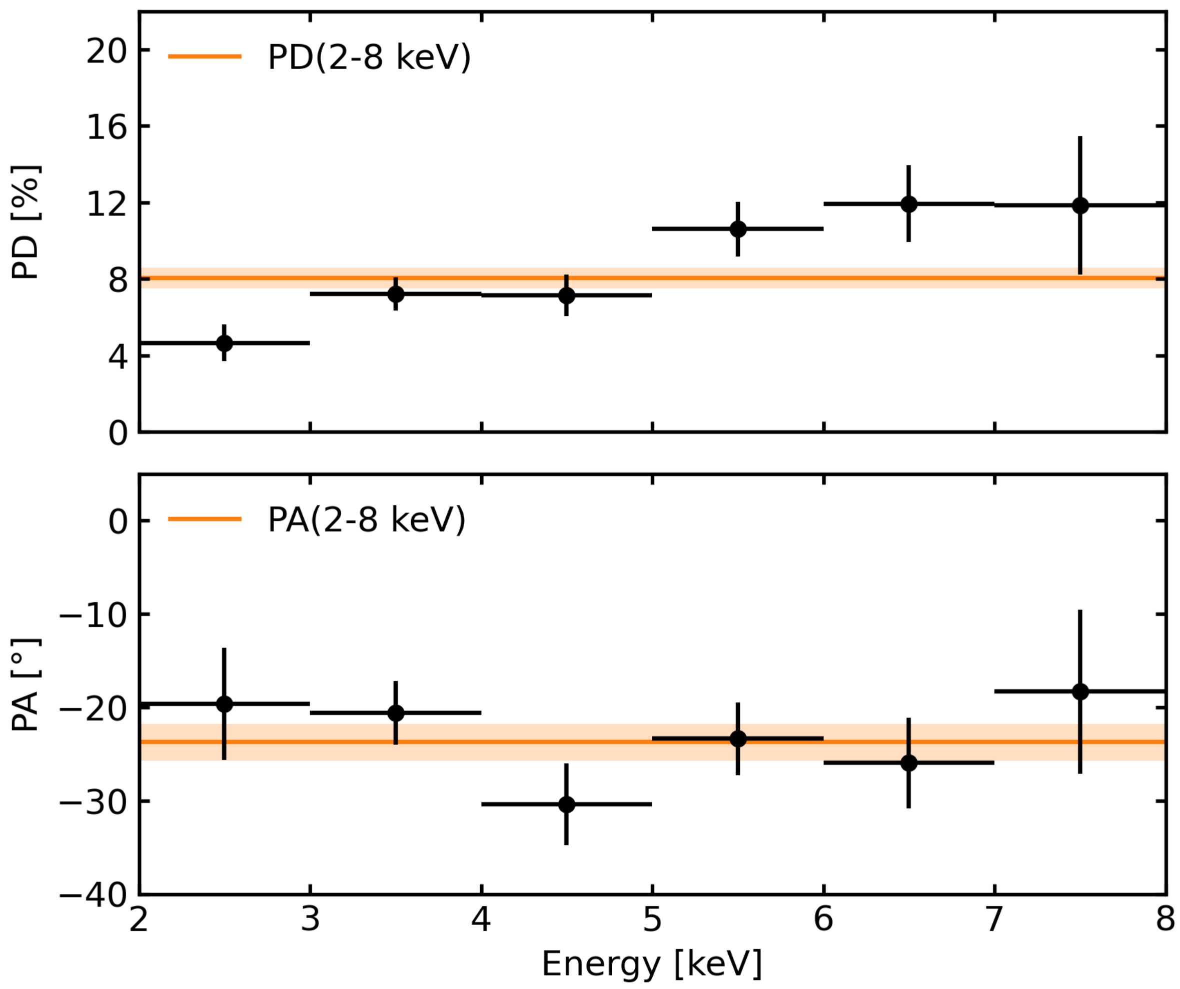

Source	Class / state	PD (2-8 keV)
GS 1826−238	atoll, soft	< 1.3%
4U 1820−303	atoll, soft	< 1.3%
XTE J1701−462	Z, NB/FB	< 1.5%
Sco X-1	Z	1.0 ± 0.2%
Cir X-1	NS-LMXB	1.4 –1.6 %
GX 9+9	atoll, soft	1.4 ± 0.3%
GX 13+1	dipping	1.4 ± 0.3%
Cyg X-2	Z, NB	1.8 ± 0.3%
4U 1624−49	dipping atoll	3.1 ±0.7%
GX 5−1	Z, HB	4.3 ± 0.3%
XTE J1701−462	Z, HB	4.6 ±0.4%
4U 1822−37	**eclipsing ADC**	**8.0 ± 0.7 %**
2S 0921−630	**eclipsing ADC**	**8.5 ± 1.6 %**
AXJ1745.6–2901	**eclipsing/dipping**	**14.7 ± 4.0%**

Spectro-polarimetric analysis

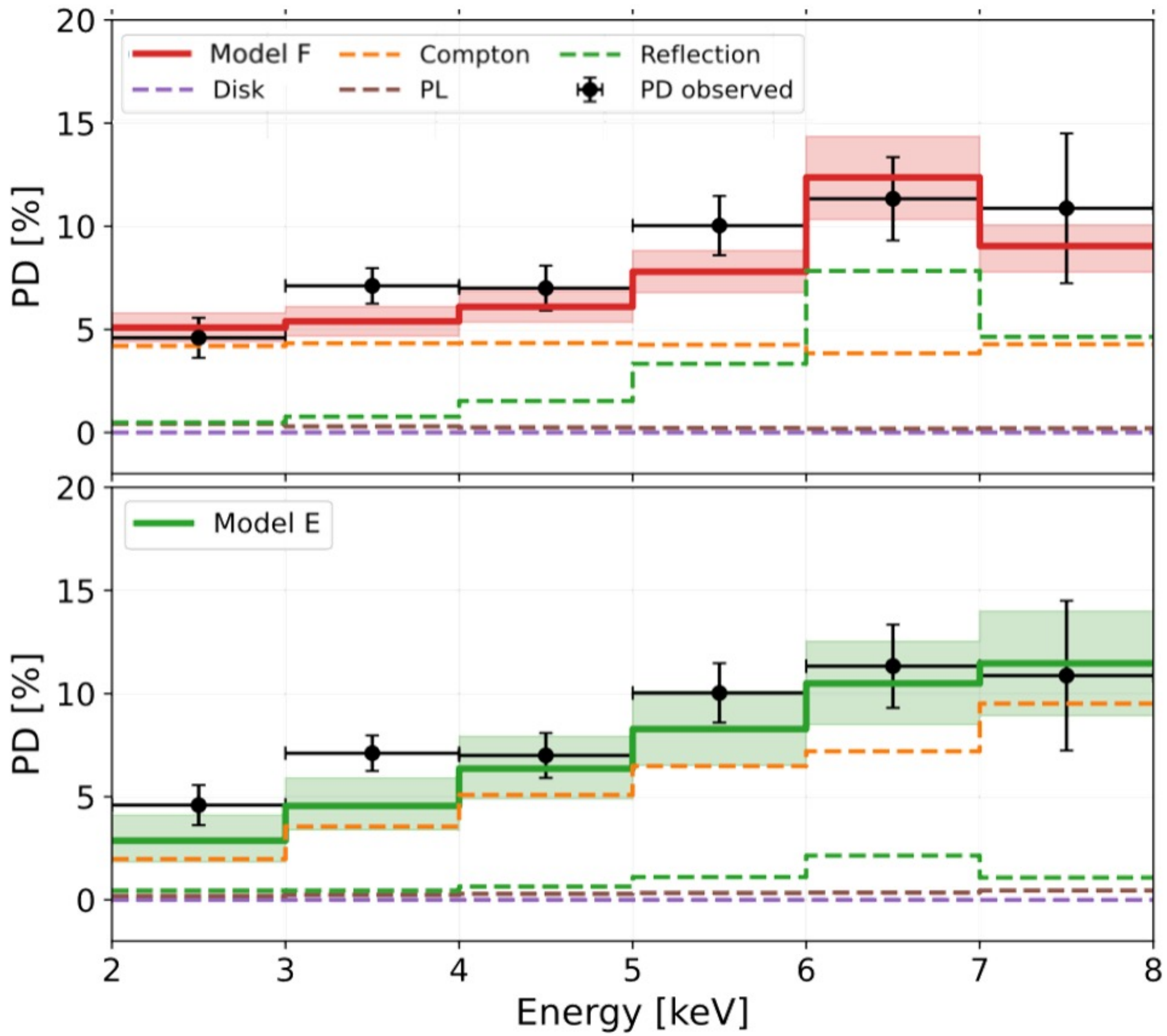

Model F: Polconst× (thcomp×bbodyrad +power−law) + Pollin × (relconv × rfxconv)

		Reflection	Compt + PL
Model F	$PD_{2\,keV}$ (%)	0.15	4.7 ± 0.7
	α_{PD} (% keV^{-1})	0.13 ± 0.04	–
	PA (°)	−27 ± 2	

Unrealistically high reflection PD, around 70–80 %

Model E : Pollin × (thcomp×bbodyrad +power−law) + Polconst × (relconv × rfxconv)

		Reflection	Compt + PL
Model E	$PD_{2\,keV}$ (%)	[20]	1.4 ± 1.4
	α_{PD} (% keV^{-1})	–	1.66 ± 0.45
	PA (°)	−26.8 ± 2.0	

More conservative option

The increase of total PD is robust but the component split is not unique

Phase resolved analysis

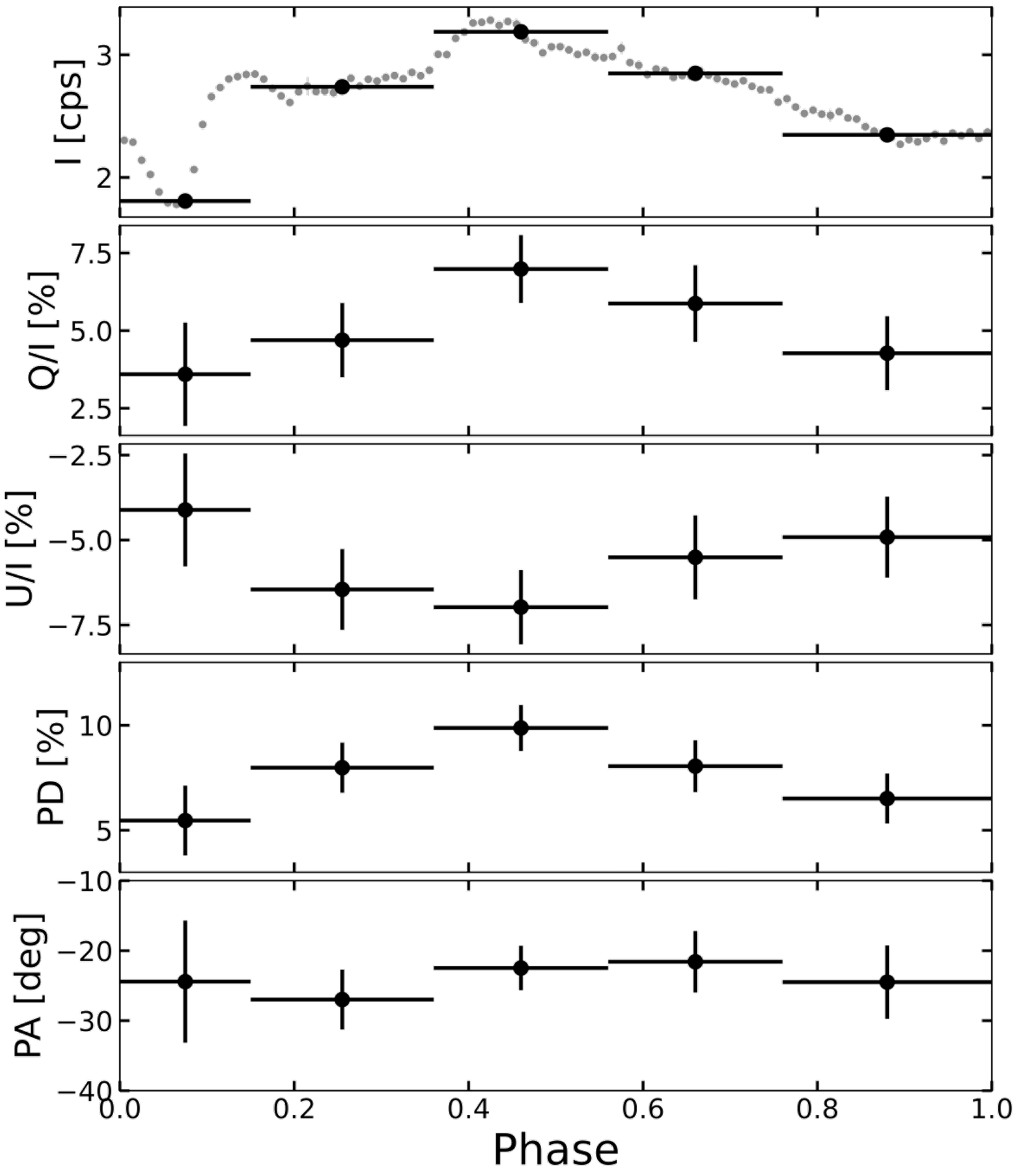

The PD decreases during the eclipse and the PA remains stable

Phase	PD (%)	PA (deg)
0.00-0.15	5.5 ± 1.7	-24.4 ± 8.7
0.15-0.36	7.98 ± 1.2	-27.0 ± 4.3
0.36-0.56	9.9 ± 1.1	-22.5 ± 3.2
0.56-0.76	8.1± 1.2	-21.6 ± 4.4
0.76-1.00	6.5 ± 1.2	-24.5 ± 5.2

Phase resolved analysis

In other high-inclination sources, the PD increases during dips/eclipses

GX 13+1

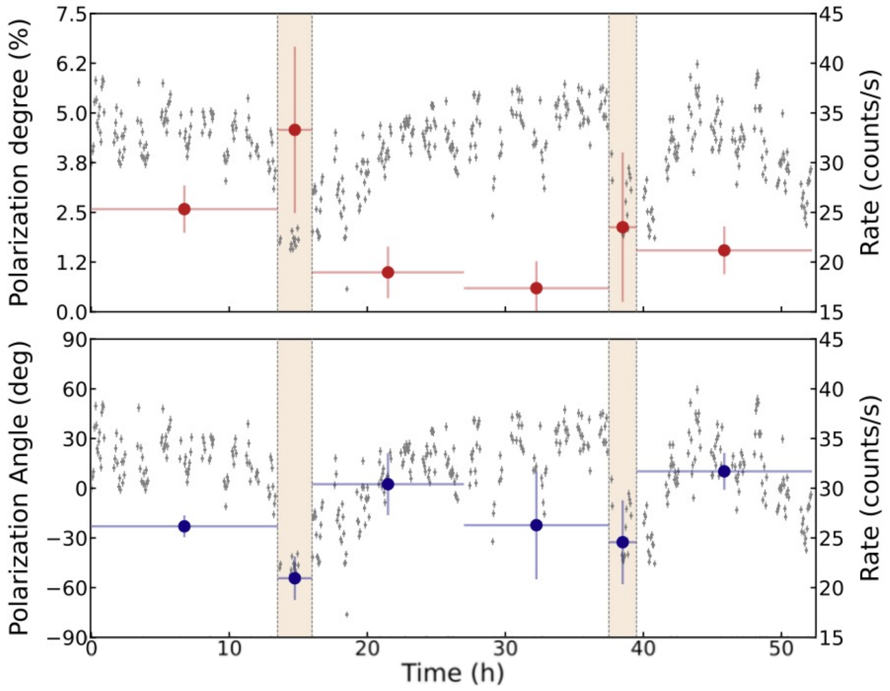

Di Marco et al 2024

2S 0921–630

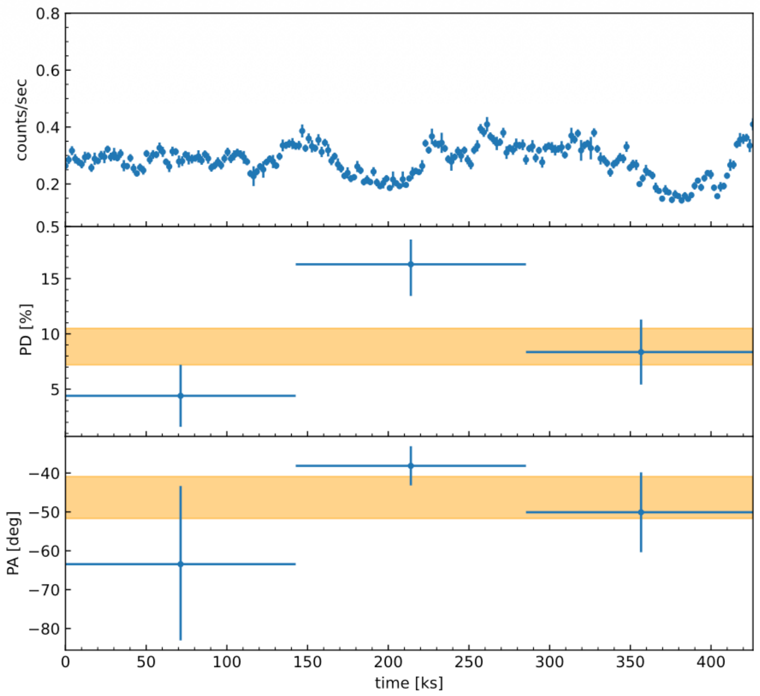

Tomaru et al 2025

AX J1745.6–2901

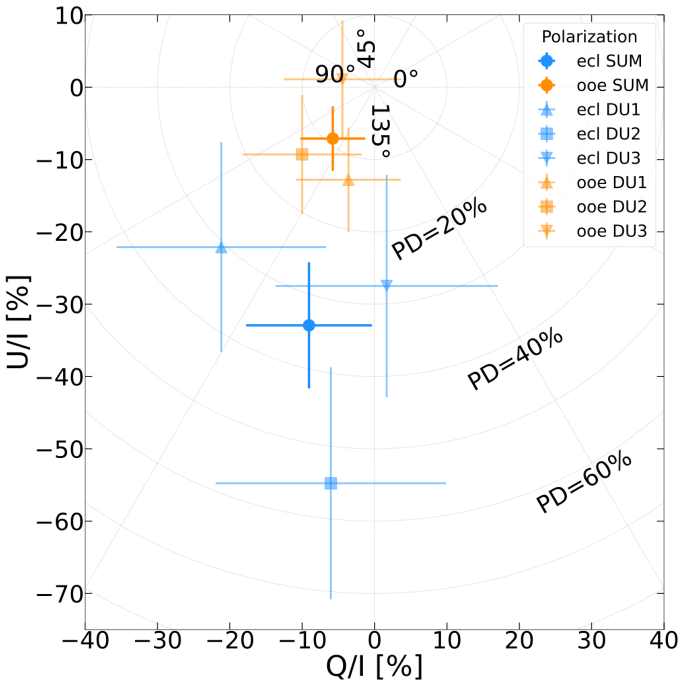

Mikusincova et al 2025

Dips/eclipses may preferentially obscure a less polarized spectral component

Spectrum during the eclipse

The spectral shape during the eclipse is consistent with the average spectrum

Eclipse spectrum

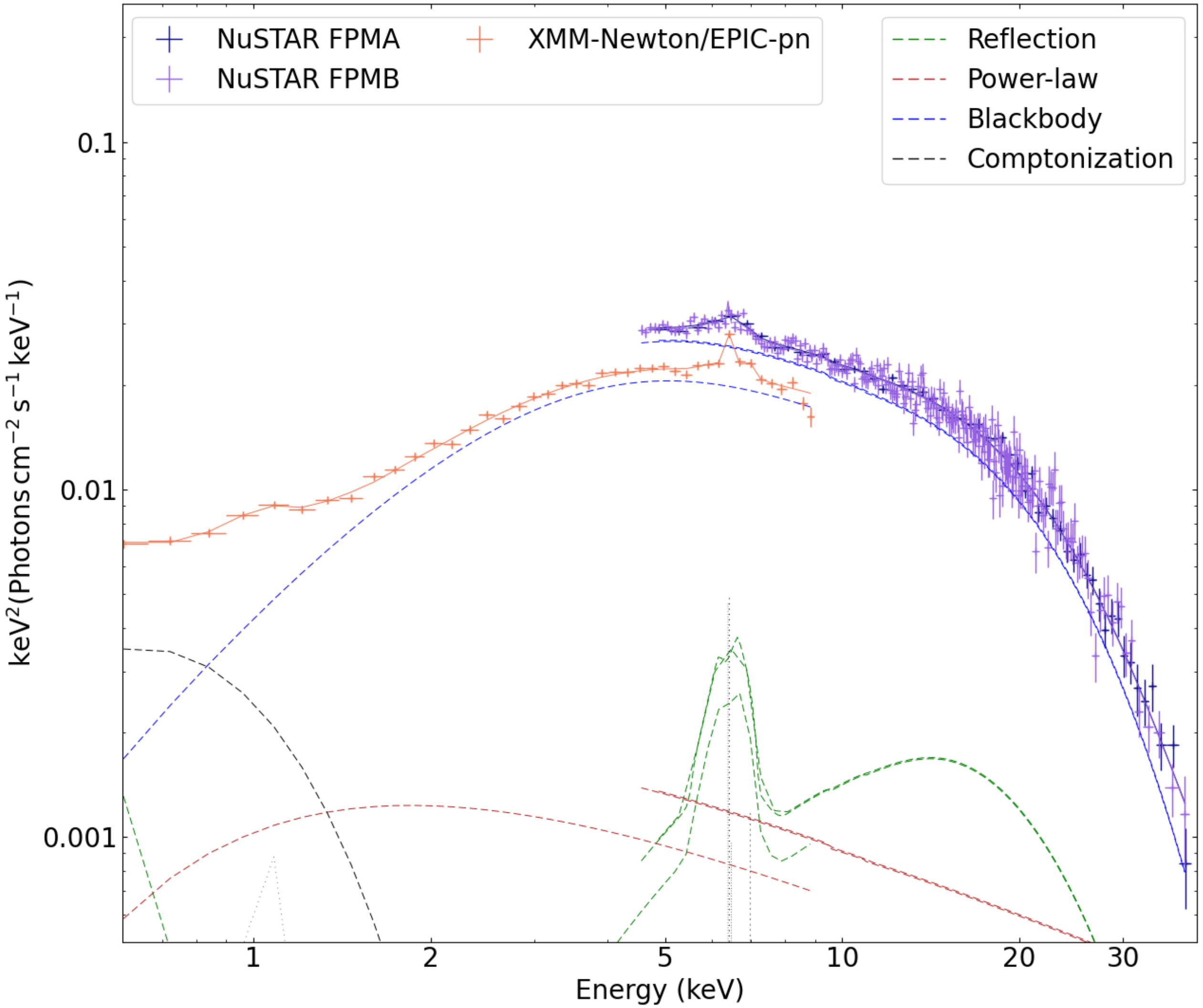

Average spectrum

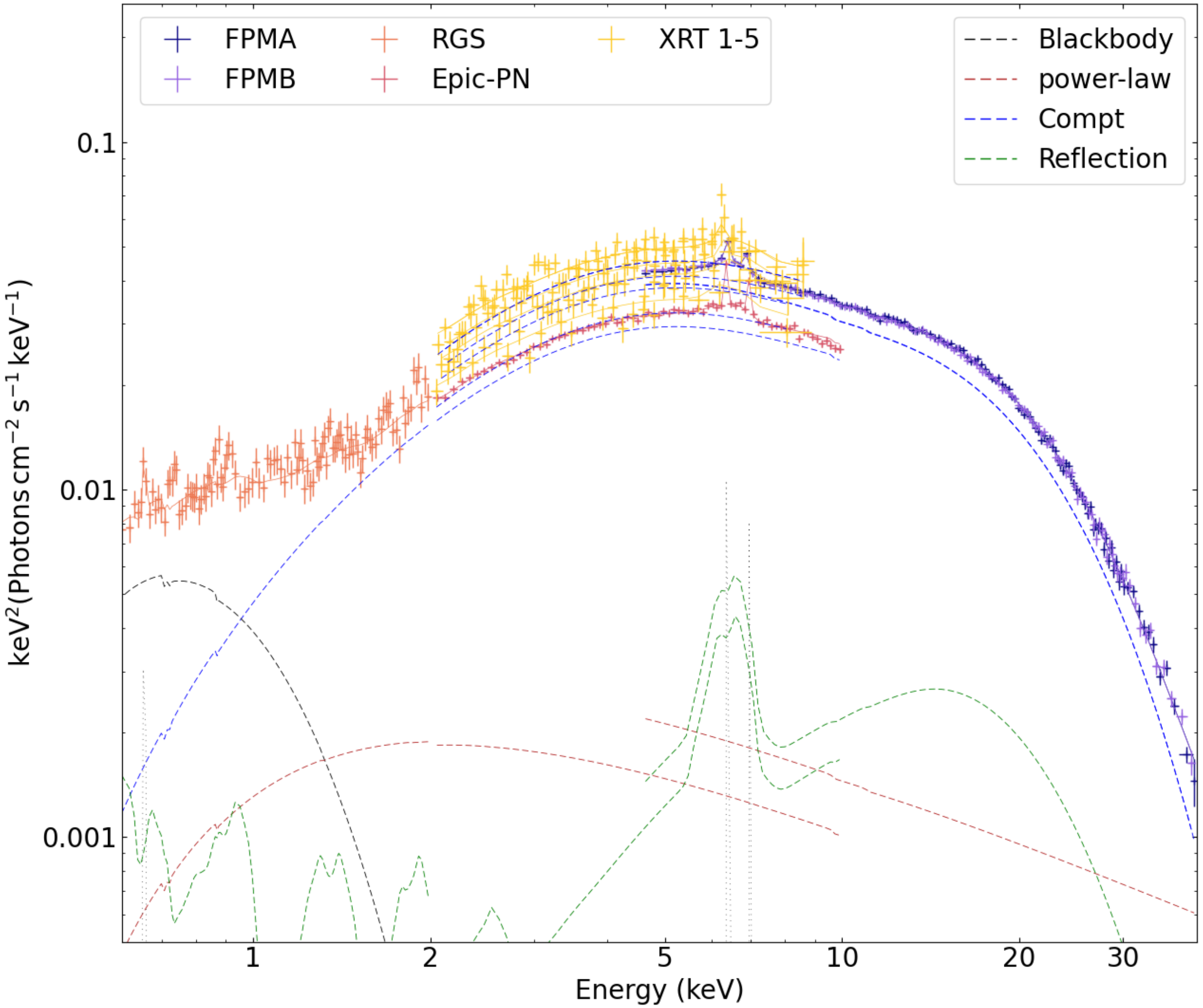

Geometrical Interpretation

Nitindala et al. 2025 showed that the regions producing the most favorable scattering angles correspond to low opening angles ($\alpha_w \sim 25°$).

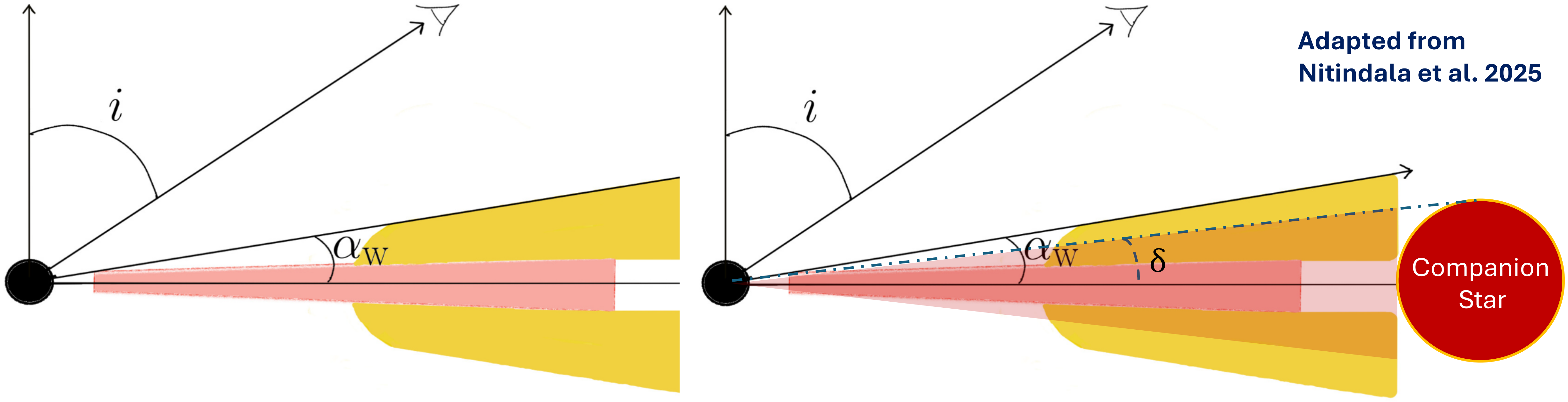

PD Maximum for $\alpha_w \sim 25°$

The eclipse obscures an angle of $\delta \sim 16°$

During the eclipse the companion partially removes the most efficient polarizing region

Summary of the results

Spectroscopy and polarimetry give a consistent picture:

4U 1822−37 is observed through an extended scattering medium that shapes the observed X-ray emission and polarization.

We measure a **high average polarization of PD = 8.0 % $\pm$ 0.7 %.**
The PD increases with energy, while the PA remains stable

During the eclipse the PD decreases, but the PA does not rotate.
The eclipse obscures the low-latitude region that is most efficient at producing polarized scattering.

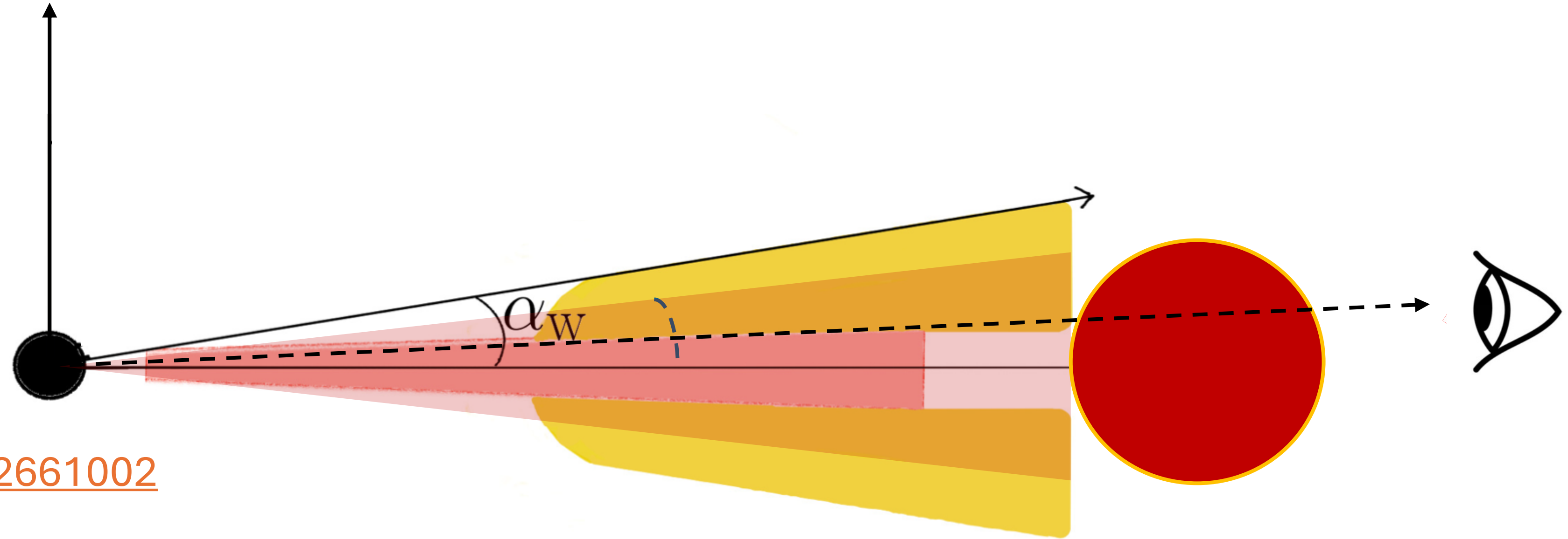

Work accepted in A&A (2026)
https://doi.org/10.1051/0004-6361/202661002

Thank you!

EXTRA SLIDES

EXTRA SLIDES – Pulsed profile

Pulse profile between 5-8 kev

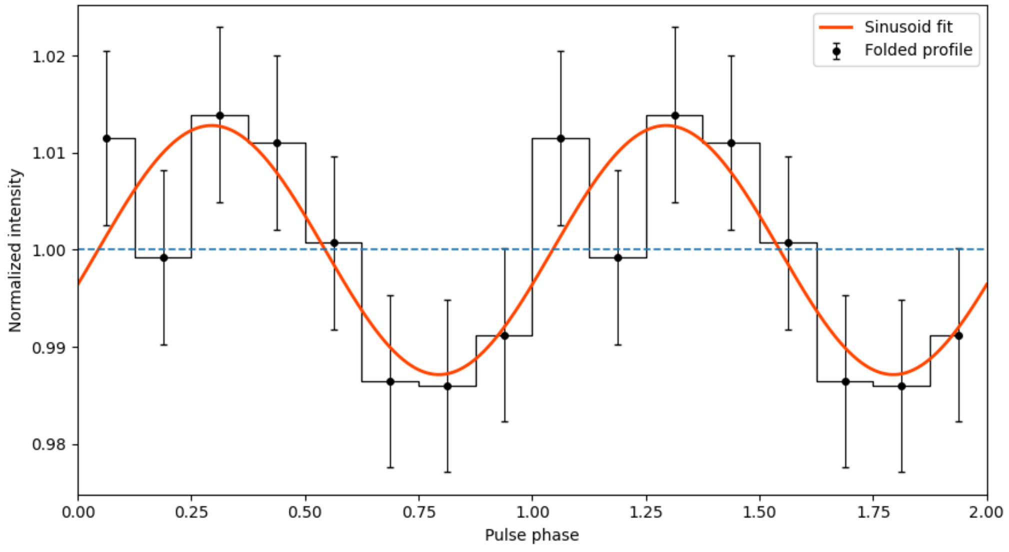

===== SINUSOID vs CONSTANT =====
Delta chi2 = 8.244 for 2 dof
p-value = 1.621e-02
Significance of modulation ≈ 2.40 sigma

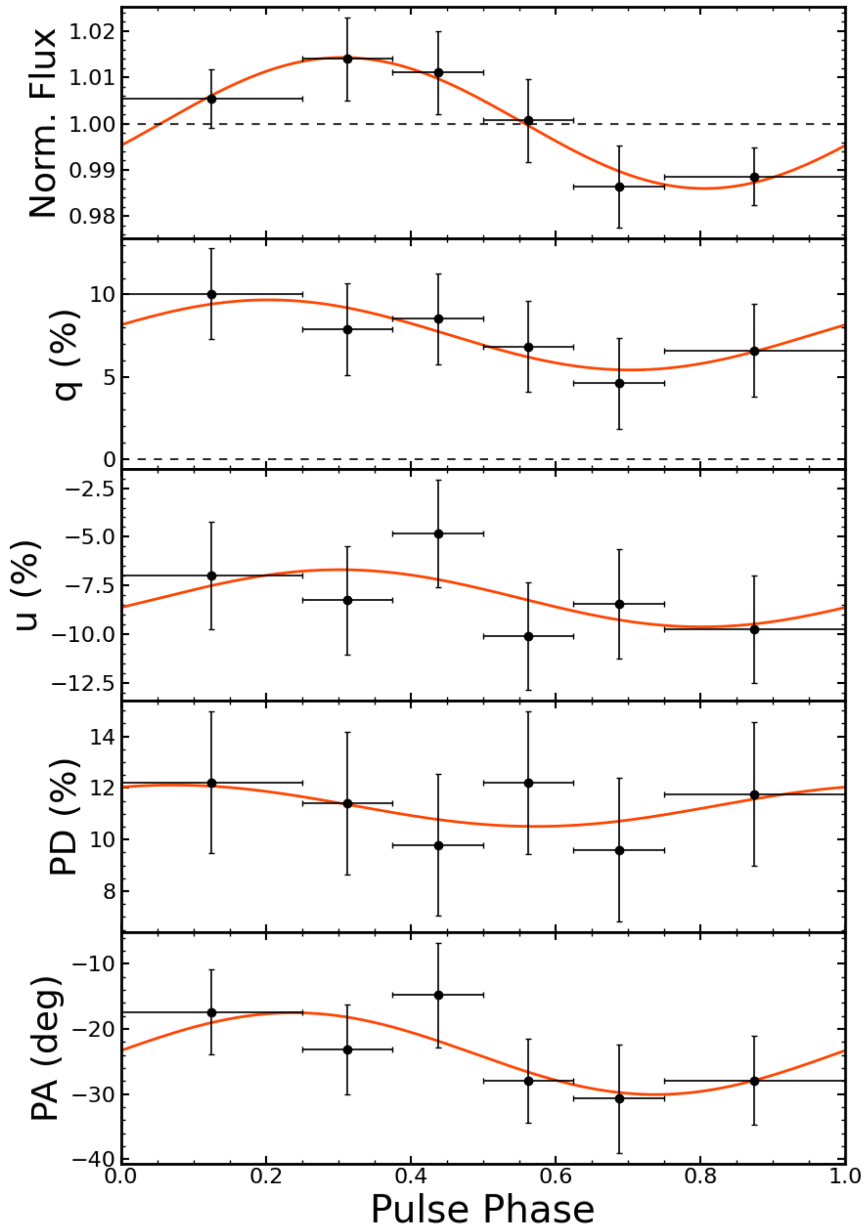

EXTRA SLIDES – XRISM (Sameshima, Tsujimoto & Uemura (2026))

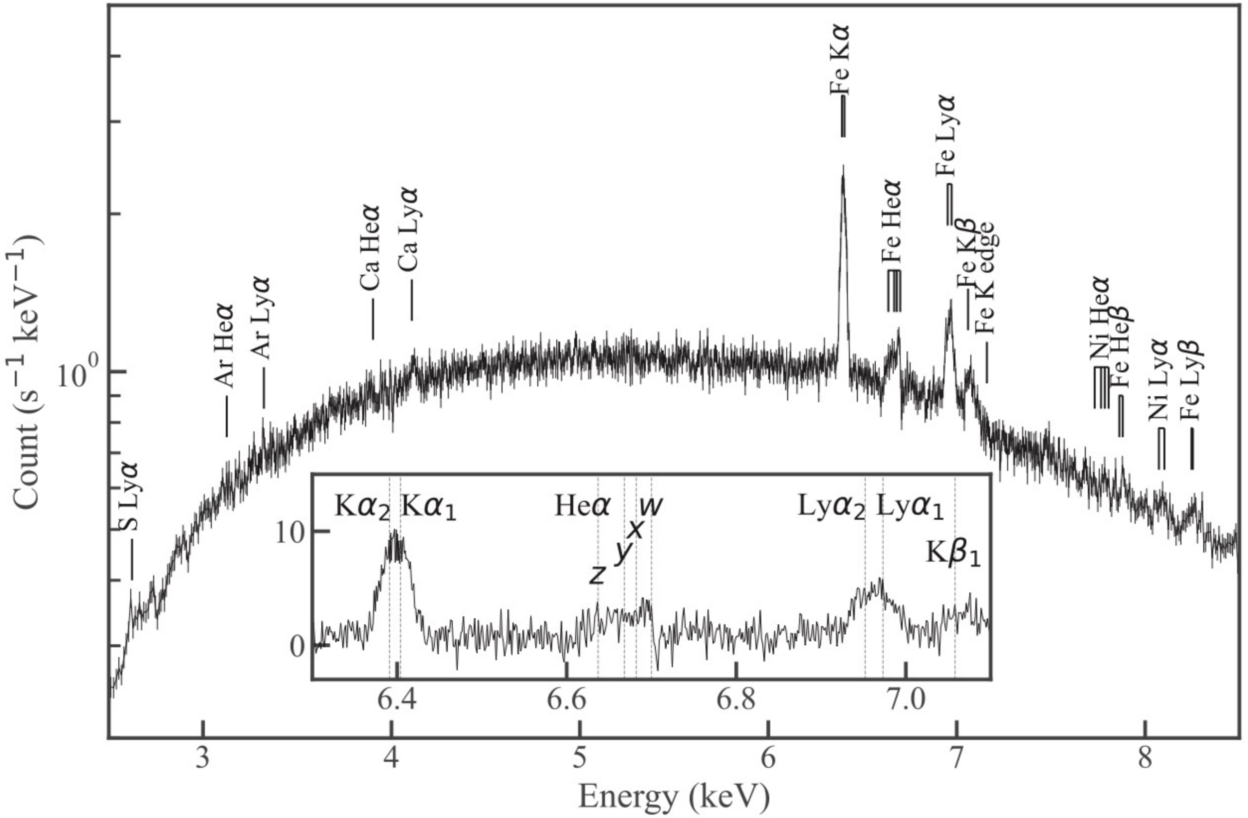

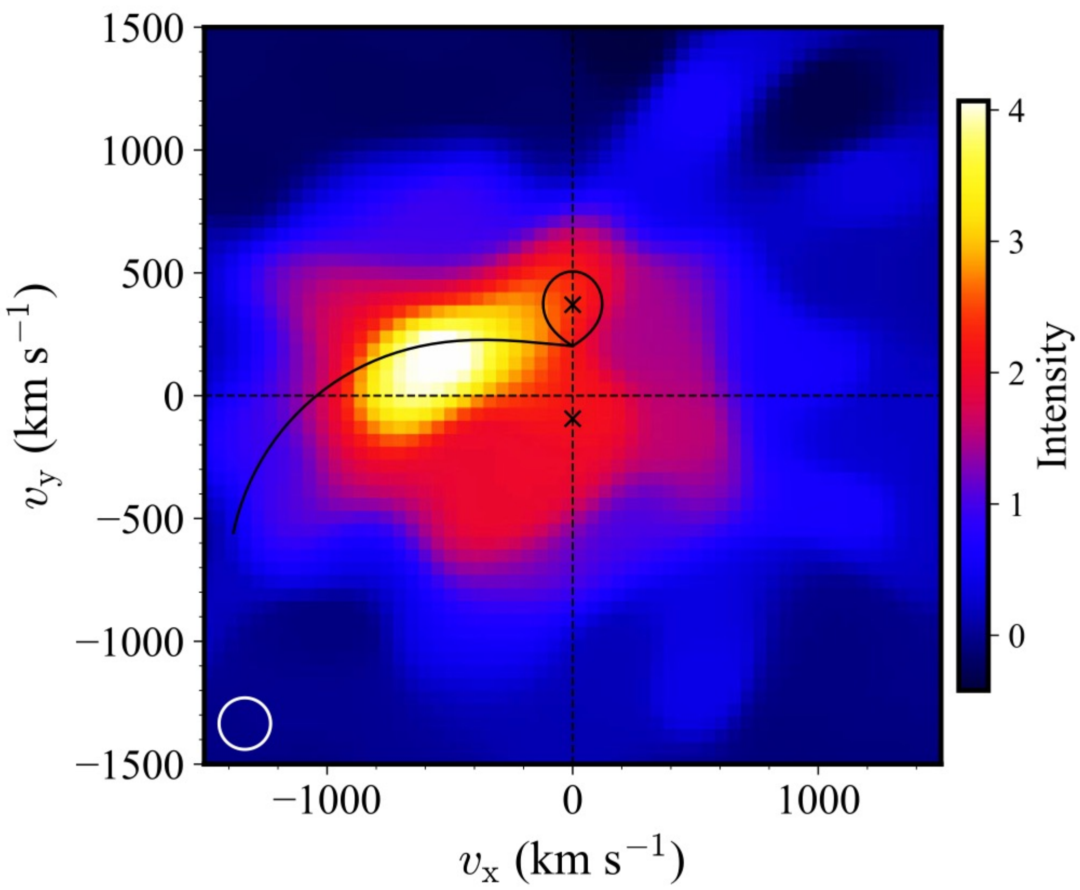

- Emission localized near the **accretion stream–disc overflow**
- Distinct from the **inner-disc broadband reflection**
- Narrow Fe Kα variability cannot explain the eclipse PD decrease

Fig. 8. Velocity map of the Fe Kα line. The position of the NS, the companion star, the Roche lobe around it, and the ballistic trajectory from L1 are shown. The velocity resolution corresponding to the line spread function is shown at the bottom left.

EXTRA SLIDES – Magnetic Field

Ghosh & Lamb (1979) equation, which links the **spin-period derivative** of the NS, its **magnetic field** and its **luminosity**

$$-\dot{P} = 5.0 \times 10^{-5} \mu_{30}^{2/7} n(\omega_s) M_1^{-3/7} I_{45}^{-1} \left(PL_{37}^{3/7}\right)^2 \mathrm{s\,yr}^{-1}.$$

In this relation, M1 is the NS mass I45 is the NS moment of inertia, and P is the spin period of the source, that is, 0.5915669 s (Mazzola et al. 2019)."

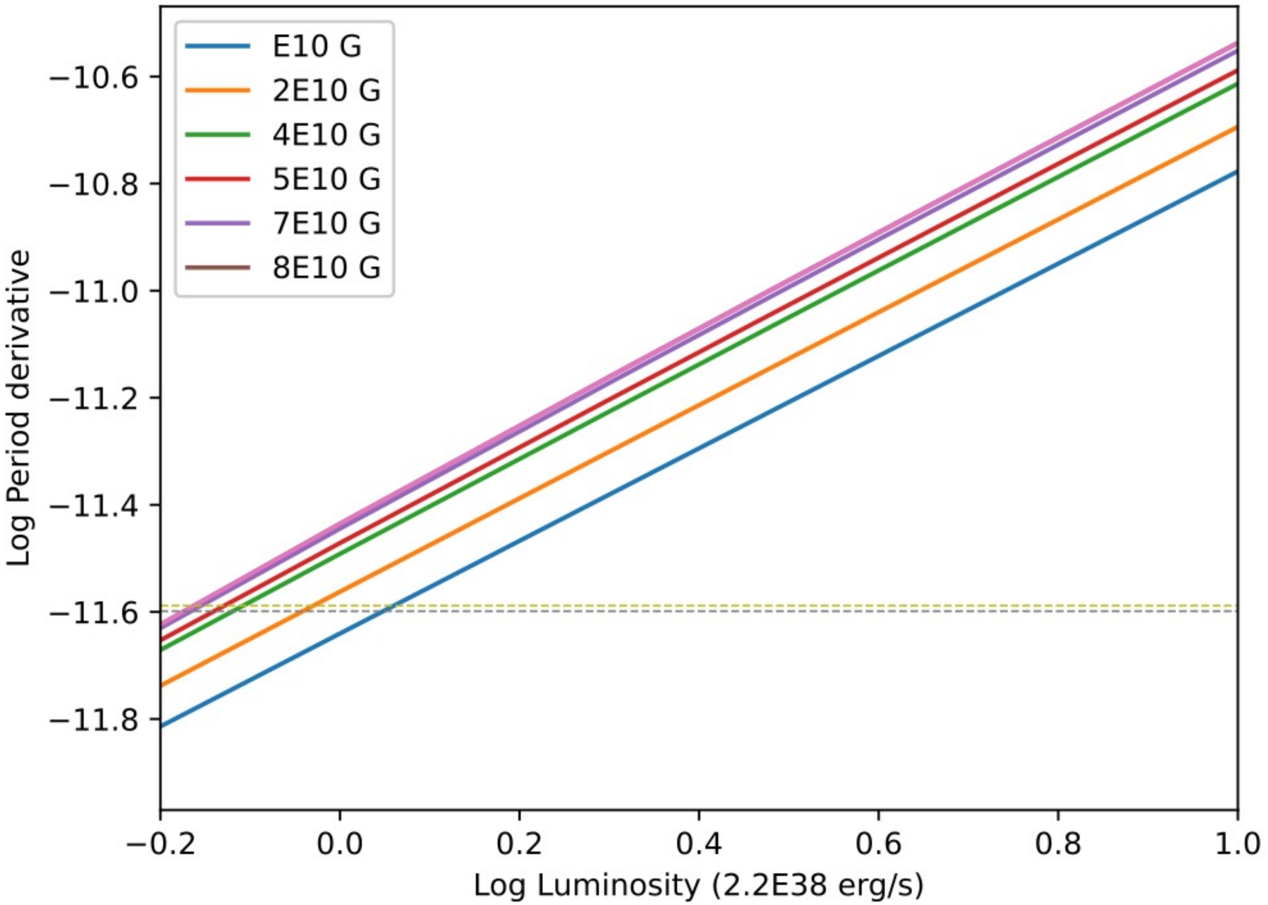

Derivative of the spin period as a function of luminosity for different values of the magnetic field.

EXTRA SLIDES – How the pulsations survive

Extendend optically thick Corona (τ = 20)

$F = \mathrm{F_0 e}^{-\tau}$, should be extremely small because of τ≃20.
Random Walk : Number of steps to escape
$N = max(\tau, \tau^2) \simeq \tau^2 \simeq 40$
Travelled space $N\lambda = \tau^2\lambda$,

ADC with $\mathrm{R_{ADC}} = 5.7\times10^{10} cm$ and τ≃20:
$\tau = n_e \, \sigma_\mathrm{T} \, R_\mathrm{ADC}$,
we find $n_e \simeq 5 \times 10^{14}\ \mathrm{cm}^{-3}$, λ≃3 × 10^9 cm,

Average delay of the escaping photons
$\mathrm{t_d} = \tau^2\lambda/c \simeq 40s$,
the spread in the arrival times of the coherent photons
$$\boldsymbol{\Delta t = \frac{\tau\lambda}{c} \simeq 2s.}$$

NO coherent pulsations

Extendend optically thin Corona (τ = 0.01)

No Random walk, 1% of photons being scatterd
$n_e \simeq 3 \times 10^{11}\ \mathrm{cm}^{-3}$ and τ ≃0.01
the mean free path is $\lambda \sim 5{\times}10$cm

Averange delay of the escaping photons is
$\tau\lambda/c \simeq 2s.$
Spread in the arrival times depends on the travelled length l in ADC.

Scattered in the outer region l= R_ADC
$\Delta t_\mathrm{max} = R_\mathrm{ADC}/c \sim 2s$

Scatterd in inner regions $R = 10^{10}$cm,
Δt =0.3 s

Allow coherent pulsations

Geometrical Interpretation

$$\frac{R_{L,2}}{a} \simeq 0.27$$

$$\delta = \arcsin\left(\frac{R_{L,2}}{a}\right) \simeq 15.7°$$

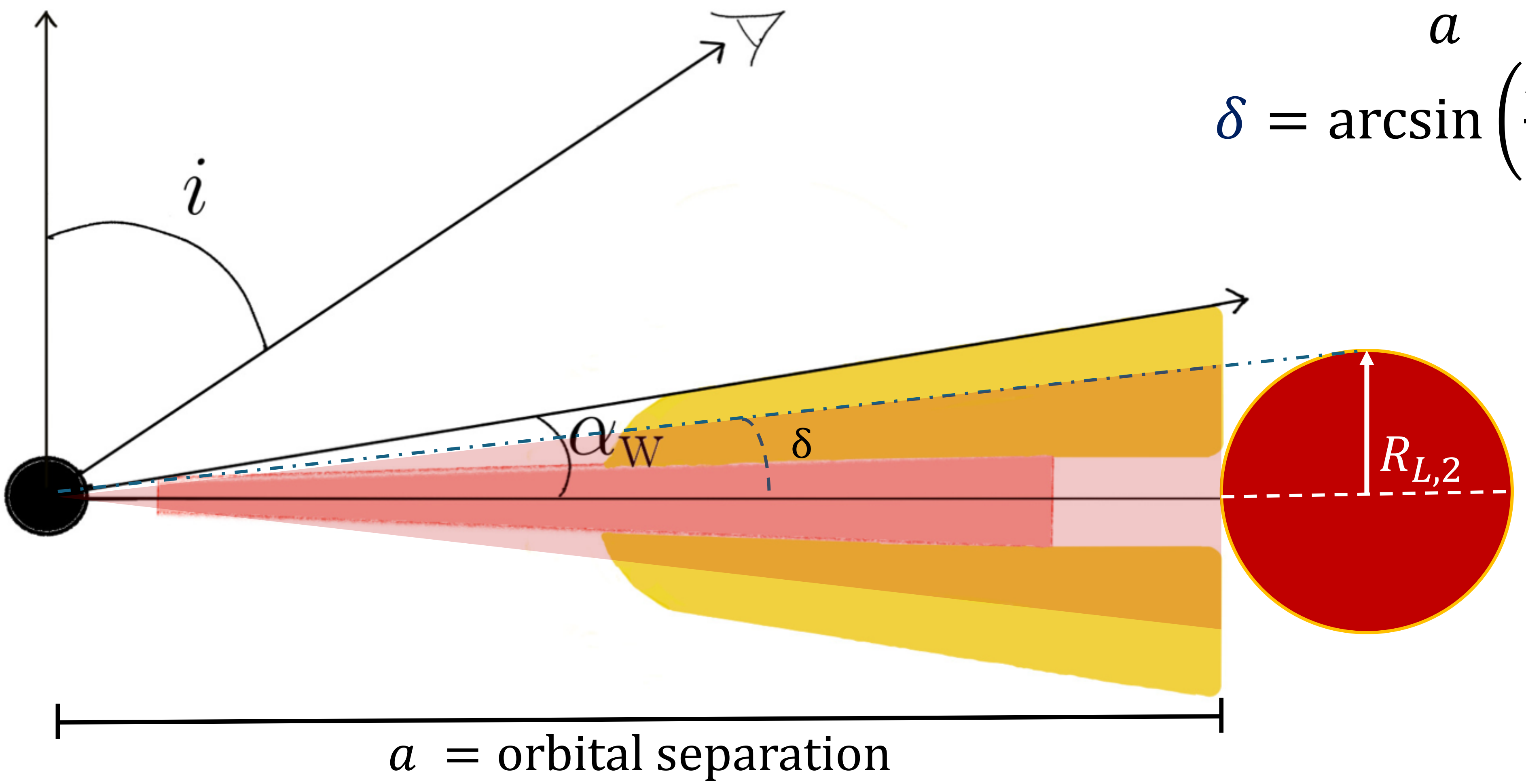

Energy range	PD (%)	PA
2–8 keV	7.9 ± 0.6	−24° ± 2°
2–3 keV	4.6 ± 1.1%	−18° ± 6°
3–4 keV	7.1 ± 0.9%	−21.° ± 4°
4–5 keV	7.0 ± 1.1%	−30° ± 5°
5–6 keV	10.1 ± 1.4%	−24° ± 4°
6–7 keV	11 ± 2%	−26° ± 5°
7–8 keV	11 ± 4%	−17° ± 9°

Energy range	Flux contribution			
	Disk	Comp.	PL	Refl.
2–8 keV	< 0.1%	88.5%	5.2%	5.3%
2–3 keV	0.2%	88.6%	8.7%	2.2%
3–4 keV	< 0.1%	91.3%	6.2%	2.2%
4–5 keV	< 0.1%	91.6%	5.2%	3.2%
5–6 keV	< 0.1%	89.9%	4.6%	5.5%
6–7 keV	< 0.1%	81.2%	3.9%	10.7%
7–8 keV	< 0.1%	90.4%	4.3%	5.4%

Model	Parameters	Value		χ^2/dof
Model A	PD (%)	6.8 ± 0.5		1411/1337
	PA (°)	−24 ± 2		
Model B	$PD_{2\,keV}$ (%)	2.4 ± 1.3		1398/1336
	α_{PD} (% keV^{-1})	1.5 ± 0.4		
	PA (°)	−24 ± 2		
		Refl.	Compt.	
Model C	PD (%)	[20]	6.3 ± 0.5	1417/1337
	PA (°)	−26 ± 2		
Model D	$PD_{2\,keV}$ (%)	[15]	< 3.1	1403/1335
	α_{PD} (% keV^{-1})	< 7	$1.7^{+0.3}_{-0.8}$	
	PA (°)	−27 ± 2		
Model E	$PD_{2\,keV}$ (%)	[20]	1.4 ± 1.3	1403/1336
	α_{PD} (% keV^{-1})	–	1.7 ± 0.5	
	PA (°)	−27 ± 2		
Model F	$PD_{2\,keV}$ (%)	[15]	4.7 ± 0.7	1407/1336
	α_{PD} (% keV^{-1})	13 ± 4	–	
	PA (°)	−27 ± 2		

Notes. Values fixed during the fit are reported in square brackets. For Models C–F, the power-law polarisation is tied to that of the Comptonised component.

Component	Parameter	Model	
		Model 1#	Model 2#
TBabs	N_H (10^{22} cm^{-2})	0.08 ± 0.04	0.132 ± 0.006
edge	E (keV)	10.9 ± 0.2	$11.0^{+0.2}_{-0.3}$
	τ (10^{-2})	1.5 ± 0.5	$1.1^{+0.5}_{-0.2}$
edge	E (keV)	9.68 ± 0.09	9.6 ± 0.2
	τ (10^{-2})	$2.7^{+0.5}_{-0.4}$	2.0 ± 0.4
gaussian	E (keV)	6.34 ± 0.01	$6.324^{+0.023}_{-0.005}$
	σ (eV)	92 ± 20	< 7
	Norm(10^{-4})	(3.8 ± 0.3)	(2.0 ± 0.2)
gaussian‡	E_{line} (keV)	6.40 ± 0.02	6.39 ± 0.02
	σ (keV)	linked†	linked†
	Norm(10^{-4})	5.2 ± 0.5	2.9 ± 0.4
gaussian	E (keV)	5.8 ± 0.1	–
	σ (keV)	0.9 ± 0.1	–
	Norm($\times 10^{-3}$)	1.2 ± 0.2	–
gaussian	E (keV)	6.87 ± 0.02	$6.91^{+0.09}_{-0.03}$
	σ (keV)	linked†	linked†
	Norm(10^{-4})	2.34 ± 0.19	$9.3^{+1.8}_{-1.5}$
gaussian‡	E_{line} (keV)	6.94 ± 0.03	6.98 ± 0.03
	σ (keV)	0.11 ± 0.02	$0.011^{+0.050}_{-0.003}$
	Norm(10^{-4})	3.7 ± 0.5	2.1 ± 0.4

Model 1: constant*TBabs*2edge*(5gauss + bbodyrad + thcomp*bbodyrad)
Model 2: constant*TBabs*2edge*(expabs*powerlaw + relconv*rfxconv*thcomp*bbodyrad + 4gauss + bbodyrad + thcomp*bbodyrad)

Component	Parameter	Model	
		Model 1#	Model 2#
bbodyrad	kT_{bb} (keV)	0.193 ± 0.013	$0.179^{+0.002}_{-0.003}$
	norm (10^3)	1.2 ± 0.5	$1.8^{+1.0}_{-0.1}$
EXPABS	E_{cut}(keV)	-	kT_{bb}
POWERLAW	Index	-	$1.72^{+0.02}_{-0.04}$
	N(10^{-3})	-	8.9 ± 0.6
thcomp	Γ_τ	1.373 ± 0.017	$1.282^{+0.002}_{-0.005}$
	kT_e (keV)	4.44 ± 0.03	4.186 ± 0.007
	cov_frac	0.78 ± 0.03	$0.647^{+0.001}_{-0.009}$
bbodyrad	kT_{bb} (keV)	1.23 ± 0.03	$1.351^{+0.006}_{-0.003}$
	norm	24.1 ± 2.0	$15.94^{+0.04}_{-0.11}$
relconv	Index1	–	$2.4^{+0.2}_{-0.1}$
	Incl (deg)	–	82.5^*
	R_{in} (R_g)	–	59^{+7}_{-9}
	R_{out} (10^3 R_g)	–	1.0^*
rfxconv	rel_refl	–	-0.62 ± 0.03
	Fe_{abund}	–	$1.0^{+0.40}_{-0.02}$
	$\log(\xi/\mathrm{erg\,cm\,s^{-1}})$	–	2.02 ± 0.02
gaussian	E (keV)	0.653 ± 0.002	0.654 ± 0.002
	σ (keV)	< 0.21	$0.002^{+0.003}_{-0.001}$
	Norm (10^{-4})	1.0 ± 0.3	1.3 ± 0.7
gaussian	E (keV)	0.569 ± 0.001	$0.5690^{+0.0008}_{-0.0012}$
	σ (10^{-3} keV)	2.4 ± 0.6	$1.9^{+1.0}_{-0.8}$
	Norm (10^{-4})	5.3 ± 1.7	7.8 ± 1.8
	χ^2/dof	1167/983	1123/979

Unabsorbed flux (0.1–100 keV) 1.37 ×10−9 erg s−1 cm−2.
Assuming a distance of 6.1 kpc (Arnason et al. 2021), luminosity of 6.1 ×10^36 erg s−1